

Supplementary Information:

Pressure effects on collective density fluctuations in water and protein solutions – Insights from neutron scattering experiments and molecular dynamics simulations

Daniela Russo^{1,2}, Alessio Lalon¹, Alessandra Filabozzi³ and Matthias Heyden^{4*}*

¹ Istituto Officina dei Materiali, Consiglio Nazionale delle Ricerche, Institut Laue Langevin,
38042 Grenoble, France

² Institut Lumière Matière, Université de Lyon 1, 69622 Lyon, France

³ Dipartimento di Fisica, Università di Roma Tor Vergata, I-00133 Roma, Italy

⁴ Theoretische Chemie, Max-Planck-Institut für Kohlenforschung, Kaiser-Wilhelm-Platz 1,
D-45470 Mülheim an der Ruhr, Germany

Corresponding authors: russo@ill.fr, heyden@kofo.mpg.de

Material and Methods

Neutron scattering sample preparation

A 10% wt/wt solution of lysozyme powder in D₂O buffer has been prepared. Protein was purchased from SIGMA Chemical Co in fully hydrated form and was employed without further purification. It has been dissolved in pure D₂O solvent to exchange labile hydrogen atoms, followed by lyophilization. The final solution was obtained by dissolving the protein powder in D₂O buffer with a concentration of 100 mg/ml. A 10-mM Tris buffer with a final pD = 6.0 has been used. Protein solutions have been finally stirred for 10 min at 9000 r/min at 292 K.

Large volume high pressure sample holder

The new interest and demand of the biophysical community, interested in food science and biology under extreme conditions, has pushed the development and construction of a pressure sample holder adapted to large solution volumes (0.7 cm³), which is suitable for neutron scattering experiments. The sample holder (Figure S1), made from titanium alloy, is designed to withstand pressures of up to 3 kbar, which can be extended up to 5 kbar. The cell design is also compatible with most of ILL Orange cryostats, for studies as a function of pressure and temperature. It is mounted on a sample holder stick. The pressure device has been conceived with a flat geometry. It is constituted of two manufactured titanium pieces, which are held together with height 12.9 security class screws and a thermally treated aluminum joint. The illuminated neutron window has an outer diameter of 27.8 mm and an inner diameter, the sample illuminated part, equals to 19.5 mm. The total thickness of the two illuminated titanium windows is of 11 mm, which results in a calculated transmission of the empty cell of 0.52. The cell is conceived for *in situ* measurements.

The hydrostatic pressure is achieved through a hand pump and monitored through a pressure sensor mounted on the cell. The loading, unloading and cleaning of the cell can be performed without opening the device, using capillaries connected to the pump. The actual thickness of the sample solution has been adapted to the new Brillouin Spectrometer BRISP, at ILL, and it is of 7 mm.

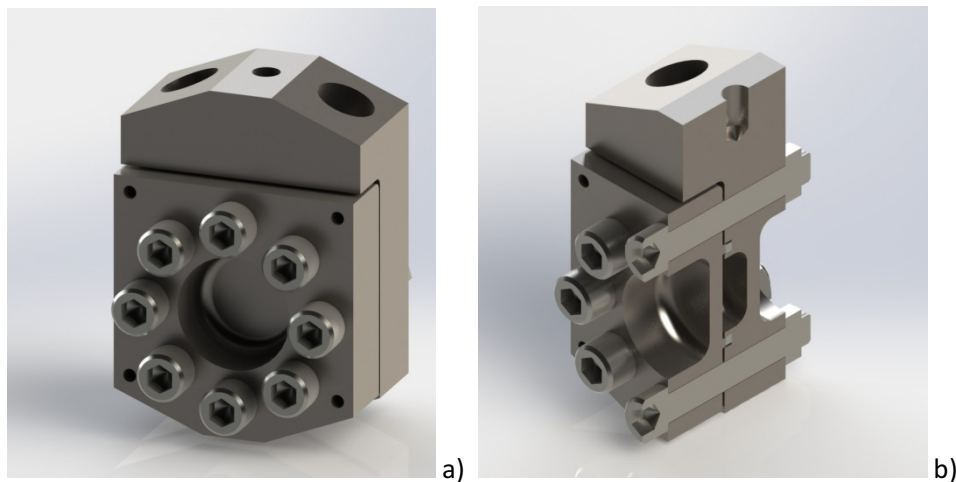


Figure S1. Large volume titanium high pressure sample holder a) face; b) section profile.

Neutron Brillouin Scattering

The measurements have been carried out on the BRISP spectrometer at the high-flux reactor ILL (Grenoble, France). The chosen configuration was: incident wavelength 0.9885 \AA , scattering angles from 1° to 13° . Therefore the dynamic Q-region was ranging from 0.2 to 1.4 \AA^{-1} . A vanadium standard measurement was used to determine the elastic instrumental energy resolution, which is well-described by a Gaussian function with $\text{FWHM} = 2.7 \text{ meV}$ (incident energy 83.7 meV), nearly constant with Q.

All data were acquired at 300 K at a pressure of 1 bar , 2 kbar and 3 kbar . The acquisition time for each sample was about 1 day . Standard procedures for the correction of raw data have been used

(correction for incident flux, sample transmission, cell scattering, environmental background, and detector efficiency). Multiple scattering contributions were evaluated with a proper simulation program and subtracted from corrected data.

To study the coherent scattering of a mixture of lysozyme and heavy water, data collected from BRISP were analyzed by fitting a two-mode model based on an elastic line plus two damped harmonic oscillators (DHOs):

In this picture, the hydration water dynamic structure factor can be expressed with $\omega = E/\hbar$ as follows:

$$S(Q, \omega) = a(Q)\delta(\omega) + [n(\omega) + 1] \left\{ \frac{a_H(Q)\Gamma_H(Q)\omega}{[\omega^2 - \Omega_H^2(Q)]^2 + [\Gamma_H(Q)\omega]^2} + \frac{a_L(Q)\Gamma_L(Q)\omega}{[\omega^2 - \Omega_L^2(Q)]^2 + [\Gamma_L(Q)\omega]^2} \right\}$$

The first term is a Dirac delta function $\delta(\omega)$ of intensity $a(Q)$, which represents both the elastic and the quasi-elastic response of the biomolecular system. The quasi-elastic component is assumed to have a negligible width compared to the instrument energy resolution. When this is not the case, a finite width function is employed instead of the delta function, (e.g. a Lorentzian function). The term $n(\omega)$ is the Bose factor, while the term between curly brackets is the sum of two DHO response functions: a high-energy term, whose parameters are identified by the subscript H , and a low-energy term, identified by the subscript L . Each DHO function is characterized by three Q -dependent parameters, that is the proper frequency $\Omega(Q)$, the damping factor $\Gamma(Q)$, and the intensity $a(Q)$. The resulting data were corrected and analyzed using the ILL LAMP programs.

All propagating modes confound with an inelastic mode at frequencies of 1-3 THz, simply because at these frequencies the acoustic excitations confound with intermolecular vibrations. At these frequencies the wavelengths are not propagating and the modes are localized. The low energy optic

like mode is probably the so-called Boson peak, which is characteristic of localized vibrational modes. The low frequency mode does not have the same origin for all materials, and in the case of water has been identified as an O-O-O bending mode. This point remains an active subject of discussion, but is not in the focus of this work and therefore not discussed in detail. Taking into account earlier published data and preliminary results, the adopted fitting strategy includes a boundary for the low energy mode ([2.6 meV]). This approach allowed a faster and more reliable fitting convergence. The Q-dependent spectra were fitted in sequence and one by one, adopting as initial condition the optimized parameters of the previous minimization.

In addition to the experimental data in Figures 3 in the main text, Figure S2 below shows a comparison of the experimental high frequency sound propagation velocities C in protein solutions and neat water at equivalent pressures. Notably, the propagation velocities are increased relative to bulk water at all pressures, while the difference decreases in the high pressure regime. We note, that the differences between propagation velocities are less pronounced in our results from molecular dynamics simulation (Figure 5C in the main text).

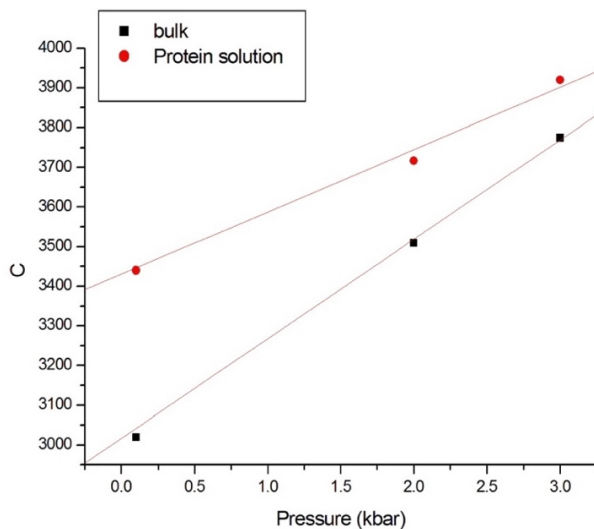


Figure S2: Comparison of the experimental high frequency sound propagation velocities at equivalent pressures for deuterated protein solutions and neat D₂O.

Figure S3 represents a direct comparison of the damping factor for lysozyme protein solutions and bulk water as a function of pressure. At both 2 and 3 kbar, the damping probed for the protein solution is higher than for bulk water. As already discussed in the main manuscript, the damping factors exhibit the most prominent characteristic differences of collective properties between the experimentally studied samples at ambient pressure. These differences even increase at elevated pressures and are likely related to interactions between hydrated protein surfaces and their surrounding hydration shell, which are modified upon compression due to the increased hydration of hydrophobic protein surface patches.

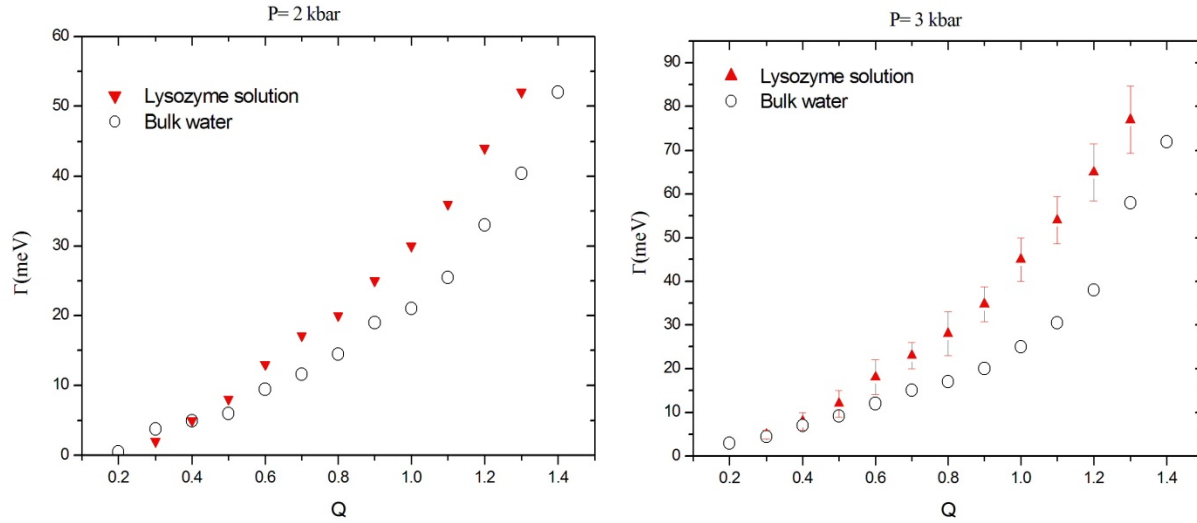


Figure S3. Comparison of the damping factors for lysozyme solution water network and neat D₂O at 2 kbar (left) and 3kbar (right).

Damped harmonic oscillator (DHO) model

The DHO serves as an analytical model to represent the data obtained from experimental and simulated coherent, inelastic scattering spectra. In addition to the signal frequency Ω , the damping factor Γ , i.e., the damping ratio Γ/Ω , has a significant influence on the fitted lineshape. For increasing damping ratios, the motion of the assumed DHO underlying the signal becomes

increasingly non-oscillatory as shown below. The differential equation underlying the DHO model function used in our analytical model is:

$$\ddot{x}(t) + \Gamma \dot{x}(t) + \Omega^2 x(t) = 0$$

In this notation, a damping ratio <1 indicates pronounced oscillatory behavior with a well-defined maximum in the spectrum close to the signal frequency. Between damping ratios of 1 and ~ 1.4 ($\sqrt{2}$) the spectral lineshape changes characteristically towards a primarily non-oscillatory behavior. The latter is indicated by a maximum amplitude at zero frequency for damping ratios $\geq \sqrt{2}$ followed by a broad high-frequency tail. Therefore, we denote damping ratios >1 as close-to-critical damping. Critical damping is obtained for a damping ratio of 2, which results in the fastest possible decay in the time domain. Damping ratios >2 , *i.e.* overdamping, result in increasingly slow relaxations in the time domain. Examples for the time evolution and the spectrum of a DHO oscillating at 25 meV for various damping ratios up to critical damping are shown below in Figure S4.

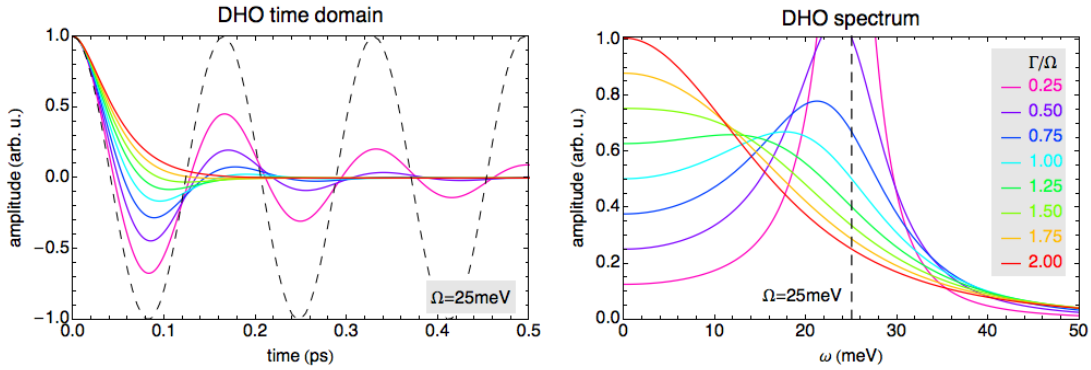


Figure S4: Time domain trajectories (left) and frequency spectra for a DHO with a fixed frequency/energy of 25 meV for varying damping ratios up to critical damping.

The analysis of the damping ratios therefore allows for a detailed assessment of the lineshape that reproduces the experimental data most accurately, in addition to a qualitative assessment of the lifetime of the oscillation. Further, the mode frequency Ω of a collective, propagating mode follows a linear dispersion relation as function of Q . Therefore, a linear increase of the damping ratio, as observed in our samples for pressurized water and the protein solutions, indicates a Q^2 -dependence of the underlying damping factor, which has been reported in the original literature¹. However, a linear increase in the damping ratio, which we use in our plots, is easier to identify than a quadratic Q -dependence of the damping factor.

Only for bulk water at ambient pressure, the damping ratio remains constant. However, we point out that this data set was obtained from the literature² and a constant damping ratio has been imposed in the underlying fit.

Molecular dynamics simulations

Molecular dynamics simulations were carried out with the GROMACS-4.6.1 software package³. The charmm22 force field parameters with CMAP corrections⁴ were used for hen egg white lysozyme (HEWL). The TIP4P-2005⁵ parameters were used for water. We chose this particular combination of protein and water force fields due to the parametrization of the TIP4P-2005 model for a wide range of pressures and temperatures⁵. Previous benchmark simulations suggest only minor effects on the protein, although the charmm22 parameters have been optimized for TIP3P water⁶. The particle-mesh Ewald summation method was employed with a grid spacing of 1.2 Å to describe long-ranged electrostatics⁷. Short-ranged interactions were shifted to zero at a cut-off distance of 9 Å. Neighbor lists were updated every 10 simulation steps with a distance cutoff of 11 Å. For equilibrations, Berendsen weak-coupling thermostats and barostats⁸ were employed at

300 K and the respective pressure using 1 picosecond time constants. For production simulations in the isothermal-isobaric ensemble we employed the Nose-Hoover thermostat⁹ and Parrinello-Rahman barostat¹⁰ instead. Protein structures were used based on the 1HEL¹¹ entry in the PDB with protonation states as predicted by the H++ software package¹² for a pH of 7.0, resulting in a net charge per protein of +8. Simulation models for concentrated protein solutions were generated via positioning of 5 randomly oriented proteins within a $(100 \text{ \AA})^3$ simulation box including 129 water molecules present in the crystal structure for each protein. The system was then neutralized with 40 chloride ions and the remaining volume was filled with 29210 water molecules. The system was then subjected to a steepest descent energy minimization for 1000 steps, prior to a 1 nanosecond dynamics simulation with position restraints applied to non-hydrogen protein atoms at a temperature of 300 K and a pressure of 1 bar. Additional pre-equilibrations at the respective target pressure (1 bar, 500 bar, 1 kbar, 2 kbar, 3 kbar and 5 kbar) were then carried out without position restraints for 1 nanosecond. The simulation time step for these equilibrations steps was set to 1 femtosecond. This was followed by 100 nanosecond production simulations using a 2 femtosecond timestep at the respective target pressures to sample the equilibrium properties of the protein solutions. Snapshots were obtained every 20 nanoseconds to generate starting points for 100 picosecond simulations in the micro-canonical ensemble (with a 1 femtosecond time step), which were used to compute longitudinal current spectra (see below). Since these simulations were used to analyze dynamic properties, the masses of hydrogens were modified to deuterium, atomic velocities were scaled accordingly, and the microcanonical simulations were preceded by a 20 picosecond equilibration with the Berendsen thermostat. Coordinates and velocities in the microcanonical simulations were saved every 8 femtoseconds, cutoffs for short-ranged interactions were increased to 11.5 Å, switching them smoothly to zero beginning at 9.0 Å.

Neighbor list cutoffs were increased accordingly to 13 Å. The analysis of structural properties was performed on the 100 nanosecond isobaric-isothermal simulations described above with light hydrogen atoms because structural properties formally do not depend on the isotope mass in classical simulations that neglect nuclear quantum effects.

Simulations of isolated HEWL proteins in solution were treated equivalently using the same initial simulation box size, however, adding only a single protein and 32422 water molecules. Bulk water systems consisted of 33049 within the same initial volume.

Simulation Analysis

Longitudinal current spectra were obtained from correlations of current densities $\vec{j}(\vec{r}, t)$ obtained from atomic positions $\vec{r}_i(t)$ and velocities $\vec{v}_i(t)$ during the 100 picosecond micro-canonical simulations of the deuterated HEWL solutions (5 proteins+ions in water) and bulk water, including weighting factors based on coherent neutron scattering cross sections β_i of the individual nuclear species.

$$\vec{j}(\vec{r}, t) = \sum_i^n \beta_i \delta[\vec{r} - \vec{r}_i(t)] \vec{v}_i(t)$$

The space-time Fourier transform is easily obtained as

$$\vec{j}(\vec{Q}, \omega) = \int e^{i\omega t} \int \sum_i^n \beta_i e^{i\vec{Q}\cdot\vec{r}} \vec{j}(\vec{r}, t) d\vec{r} dt = \int e^{i\omega t} \sum_i^n \beta_i e^{i\vec{Q}\cdot\vec{r}_i(t)} \vec{v}_i(t) dt$$

This expression was evaluated for Q-vectors corresponding to 0.2 to 4.0 Å⁻¹ with steps of 0.1 Å⁻¹. For each Q-vector length 40 vectors were selected from a discrete reciprocal space grid defined by the periodic boundary conditions of the simulation cell. After projection on the respective Q-vector to obtain the longitudinal components of the current density, the longitudinal current spectrum is

then simply obtained as the product of the complex conjugates in reciprocal space and in the frequency domain

$$I^{\parallel}(Q, \omega) = \left[\vec{J}(\vec{Q}, \omega) \frac{\vec{Q}}{|\vec{Q}|} \right] \left[\vec{J}(\vec{Q}, \omega) \frac{\vec{Q}}{|\vec{Q}|} \right]^*$$

The resulting spectra were then analyzed within the two-component damped harmonic oscillator model used for the experimental data including a ω^2/Q^2 prefactor that distinguishes the dynamic structure factor from the longitudinal current spectrum. Contour plots in Figure 5B of the main text indicate the Q-dependent longitudinal current spectra for one selected system (protein solution at 2 kbar). The fitted high-frequency peak positions of the spectra are compared in Figure 5C and 5D of the main text. High-frequency sound propagation velocities were obtained from a linear fit of the dispersion curve between 0.3 and 1.0 Å⁻¹.

Density profiles of water centers were evaluated from the 100ns simulations of isolated proteins in solution in the isothermal-isobaric ensemble. For this purpose, the environment of the protein was first discretized into voxels with an edge length of 1 Å. For each voxel element and simulation time step then the distance to the closest protein non-hydrogen atom was evaluated. Water molecules in simulation snapshots stored every 10 picoseconds were then assigned to grid voxels based on the position of the center of mass, allowing to efficiently assign their distance to the protein.

In addition, the hydrogen bond angle-based tetrahedral order parameters¹³⁻¹⁴ were computed with increasing pressure in bulk water as well as within 5 Å hydration shells (relative to closest non-hydrogen protein atom) in the protein environment.

$$q = 1 - \frac{3}{8} \sum_j^3 \sum_{k=j+1}^4 \left(\cos \psi_{jk} + \frac{1}{3} \right)^2$$

Here, the angles ψ_{jk} describe angles between vectors connecting the hydrogen bond donor/acceptor atom of the four nearest neighbor sites of a water molecule with the oxygen atom of the central water molecule. The results of this analysis are shown together with radial distribution functions of the water-center of mass for increasing pressure in Figures 6 C, D, and E.

Protein stability in the studied pressure range

The stability of lysozyme solutions under comparable conditions as used in our experimental study have been reported by Heremans & Wong¹⁵. At a protein concentration of 10% w/w, a pH of 7.4 and a buffer concentration of 2.5 mM, spectral changes of vibrational bands in the Raman spectrum were used to show virtually no changes of the protein structure up to pressures of 3.6 kbar, which includes the pressures used in our experiments¹⁵. Irreversible protein aggregation has been observed only for pressures above 5.5 kbar, which exceeds the pressure range explored in our study.

Additional studies are available for dilute lysozyme solutions under varying conditions, which may lack stabilizing or destabilizing effects due to protein-protein interactions. Tryptophan fluorescence measurements of lysozyme in solution were carried out by Li *et al.* for pressures up to 11kbar¹⁶. In this experiment, the halfway point of a reversible denaturation process has been determined as 4.3 kbar. Fluorescence polarization experiments on solutions of labeled lysozyme at pH 8 by Chrysomallis *et al.* report a volume increase between 5 and 10 kbar¹⁷, indicative of unfolding. Further, proton NMR experiments have been used to follow pressure denaturation of lysozyme under acidic conditions (pH 3.9) and elevated temperature (68.5°C) via shifts of signals from various residues in the pressure range from 1 bar to 5 kbar¹⁸. Under these comparably harsh

conditions, a 20-30% denaturation is observed at 3 kbar and a 40-50% denaturation at the maximum pressure of 5 kbar.

While our experiments were carried out up to 3 kbar, we extended the studied pressure range in our molecular dynamics simulations to pressures up to 5 kbar. In these simulations, we can monitor the protein stability directly via the root mean squared displacements (RMSD) of protein heavy atoms (all non-hydrogen atoms) relative to the crystal structure for the five simulated proteins monomers in our 10% w/w solution. Protein diffusion and tumbling of each protein monomer is removed for this analysis by a translational and rotational fit of the corresponding protein atoms with respect to the reference structure. The result shown in Fig. S5 demonstrates near-native conformations of all protein monomers over the entire simulation length ($\text{RMSD} < 2.0 \text{ \AA}$). While this result does not guarantee a thermodynamically stable folded state due to the limited sampling time of 100 ns, it proves that the results obtained from the analysis of our trajectories are representative of solutions of natively folded proteins. In addition, our simulations reproduce a previous observation obtained from quasi-elastic neutron scattering (QENS) experiments on lysozyme solutions¹⁹, which reports a reduced protein flexibility with increasing pressure. The latter is reflected by the RMSD time traces as the maximum RMSD's are decreasing with increasing pressure and the 5 distinct protein monomers show increasingly homogenous time traces at 3 and 5 kbar compared to lower pressures.

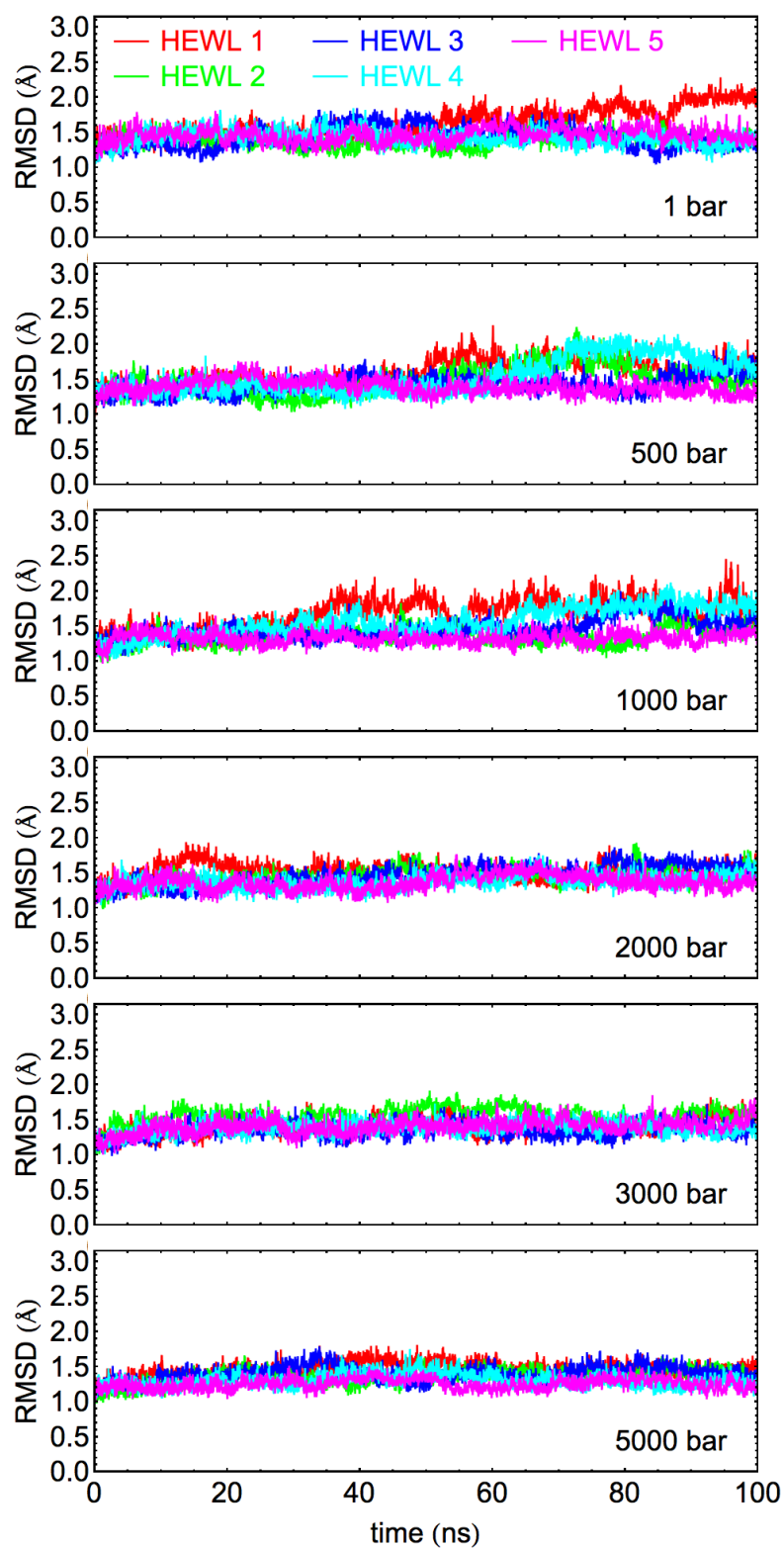


Figure S5: Protein heavy atom RMSD's after translational and rotational fitting as a function of simulation time for each monomer in the simulated 10% w/w protein solution for all simulated pressures.

Effect of pressure on pH and sidechain protonation

In the studies summarized above, the pH was determined at ambient pressure, equivalent to our experiments. Pressure-induced changes in pH are therefore not specifically considered and should be comparable between these experiments.

However, pressure-induced effects on the protonation state of the protein are potentially relevant to our simulations, where the protonation state is fixed by the topology of the employed simulation model. Pressure-induced changes in the pH of water are the result of an increased auto-ionization product for water as the ionized species occupy a smaller partial molar volume than neutral water molecules. Therefore, increased pressures result in a lower pH, as well as a lower pOH^{20} . Hence, the increased concentrations of ionized water species themselves would not directly affect the equilibrium between distinct protein sidechains. Likewise the pH/pD range relevant to our simulations corresponds to such small concentrations of the ionized species, that virtually no H_3O^+ or OH^- ions are expected in our finite size simulation box.

Instead, the same mechanism that increases the auto-ionization product of water is likely to increase the probability of weakly basic and acidic sidechains to be protonated or deprotonated, respectively. Small angle x-ray scattering experiments¹⁹ of concentrated lysozyme solutions (10% wt/wt, pH 7.5, 30mM salt) for pressures up to 1.5 kbar indicate a decrease in the coulombic repulsion between the proteins at high pressures, which would indicate a decrease of the positive charge of +8 observed at near-neutral pH's for ambient pressures. A reduced positive charge despite favorable ionization of sidechains would indicate an increased number of negatively charged sidechains.

In our simulation, all standard acidic sidechains (ASP, GLU) are already deprotonated for simulations at ambient pressure. We identified TYR 20 and 23 as potential deprotonation candidates for non-standard negative sidechains, which would reduce the total protein charge to +6. We therefore repeated our simulations of lysozyme solutions at the highest pressure of 5 kbar with this modified charge state to infer a potential influence of pressure-induced changes in the protonation state on our results.

In the following Figure S6, we compare the results for the sound propagation velocity in the concentrated protein solution (10% wt/wt) with the data shown in the main manuscript (Fig. 5C and D). We omit a comparison for the structure of the protein hydration water in dilute solutions as shown in Fig. 6 C and D as the results from simulations with the distinct protonation states were essentially indistinguishable. While not being exactly identical, the difference between the average high frequency sound propagation velocities at 5 kbar for simulations of the protein solution with the default and modified protonation states are within the statistical error bar obtained from averaging over 5 independent trajectories. Consequently, we are certain that our conclusion are not affected by pressure-induced changes in the sidechain protonation pattern for the simulated lysozyme proteins.

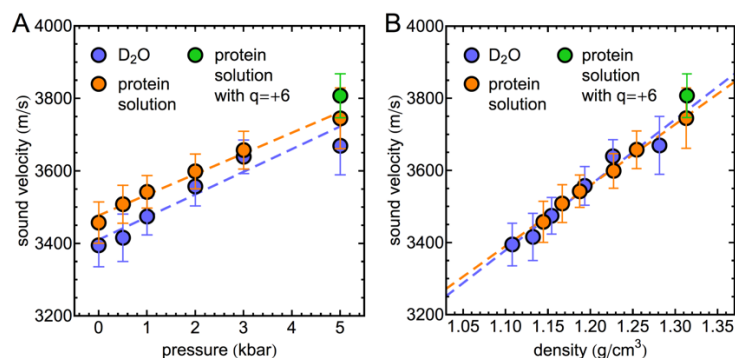


Figure S6: Same as Figure 5 in the main manuscript, however, including high frequency sound propagation velocities obtained for protein solutions with a modified protonation state at 5 kbar.

References

1. Teixeira, J.; Bellissentfunel, M. C.; Chen, S. H.; Dorner, B., Observation of New Short-Wavelength Collective Excitations in Heavy-Water by Coherent Inelastic Neutron-Scattering. *Phys Rev Lett* **1985**, *54* (25), 2681-2683.
2. Sacchetti, F.; Suck, J. B.; Petrillo, C.; Dorner, B., Brillouin neutron scattering in heavy water: Evidence for two-mode collective dynamics. *Phys Rev E* **2004**, *69* (6), 061203.
3. Hess, B.; Kutzner, C.; van der Spoel, D.; Lindahl, E., GROMACS 4: Algorithms for highly efficient, load-balanced, and scalable molecular simulation. *J Chem Theory Comput* **2008**, *4* (3), 435-447.
4. Buck, M.; Bouguet-Bonnet, S.; Pastor, R. W.; MacKerell, A. D., Importance of the CMAP correction to the CHARMM22 protein force field: Dynamics of hen lysozyme. *Biophys J* **2006**, *90* (4), L36-L38.
5. Abascal, J. L. F.; Vega, C., A general purpose model for the condensed phases of water: TIP4P/2005. *J Chem Phys* **2005**, *123* (23), 234505.
6. Cerutti, D. S.; Freddolino, P. L.; Duke, R. E.; Case, D. A., Simulations of a Protein Crystal with a High Resolution X-ray Structure: Evaluation of Force Fields and Water Models. *J Phys Chem B* **2010**, *114* (40), 12811-12824.
7. Darden, T.; York, D.; Pedersen, L., Particle Mesh Ewald - an N.Log(N) Method for Ewald Sums in Large Systems. *J Chem Phys* **1993**, *98* (12), 10089-10092.
8. Berendsen, H. J. C.; Postma, J. P. M.; Vangunsteren, W. F.; Dinola, A.; Haak, J. R., Molecular-Dynamics with Coupling to an External Bath. *J Chem Phys* **1984**, *81* (8), 3684-3690.
9. Nosé, S., A Molecular-Dynamics Method for Simulations in the Canonical Ensemble. *Mol Phys* **1984**, *52* (2), 255-268.
10. Parrinello, M.; Rahman, A., Polymorphic Transitions in Single-Crystals - a New Molecular-Dynamics Method. *J Appl Phys* **1981**, *52* (12), 7182-7190.
11. Wilson, K. P.; Malcolm, B. A.; Matthews, B. W., Structural and Thermodynamic Analysis of Compensating Mutations within the Core of Chicken Egg-White Lysozyme. *J Biol Chem* **1992**, *267* (15), 10842-10849.
12. Anandakrishnan, R.; Aguilar, B.; Onufriev, A. V., H++3.0: automating pK prediction and the preparation of biomolecular structures for atomistic molecular modeling and simulations. *Nucleic Acids Res* **2012**, *40* (W1), W537-W541.
13. Errington, J. R.; Debenedetti, P. G., Relationship between structural order and the anomalies of liquid water. *Nature* **2001**, *409* (6818), 318-321.
14. Duboue-Dijon, E.; Laage, D., Characterization of the Local Structure in Liquid Water by Various Order Parameters. *J Phys Chem B* **2015**, *119* (26), 8406-8418.
15. Heremans, K.; Wong, P. T. T., Pressure Effects on the Raman-Spectra of Proteins - Pressure-Induced Changes in the Conformation of Lysozyme in Aqueous-Solutions. *Chem Phys Lett* **1985**, *118* (1), 101-104.
16. Li, T. M.; Hook, J. W.; Drickamer, H. G.; Weber, G., Plurality of Pressure-Denatured Forms in Chymotrypsinogen and Lysozyme. *Biochemistry* **1976**, *15* (25), 5571-5580.
17. Chrysomallis, G. S.; Torgerson, P. M.; Drickamer, H. G.; Weber, G., Effect of Hydrostatic-Pressure on Lysozyme and Chymotrypsinogen Detected by Fluorescence Polarization. *Biochemistry* **1981**, *20* (14), 3955-3959.
18. Samarasinghe, S. D.; Campbell, D. M.; Jonas, A.; Jonas, J., High-Resolution Nmr-Study of the Pressure-Induced Unfolding of Lysozyme. *Biochemistry* **1992**, *31* (34), 7773-7778.
19. Ortore, M. G.; Spinozzi, F.; Mariani, P.; Paciaroni, A.; Barbosa, L. R. S.; Amenitsch, H.; Steinhart, M.; Ollivier, J.; Russo, D., Combining structure and dynamics: non-denaturing high-pressure effect on lysozyme in solution. *J Roy Soc Interface* **2009**, *6*, S619-S634.

20. Bandura, A. V.; Lvov, S. N., The ionization constant of water over wide ranges of temperature and density. *J Phys Chem Ref Data* **2006**, 35 (1), 15-30.